A&A 465, 445–456 (2007)
DOI: 10.1051/0004-6361:20066141

Astronomy & Astrophysics

On the structure of the turbulent interstellar atomic hydrogen

II. First comparison between observation and theory. Are the characteristics of molecular clouds determined early in the turbulent 2-phase atomic gas?

P. Hennebelle[1], E. Audit[2], and M.-A. Miville-Deschênes[3]

[1] Laboratoire de radioastronomie millimétrique, UMR 8112 du CNRS, École normale supérieure et Observatoire de Paris, 24 rue Lhomond, 75231 Paris Cedex 05, France
e-mail: patrick.hennebelle@ens.fr
[2] Service d'Astrophysique, CEA/DSM/DAPNIA/SAp, CE Saclay, 91191 Gif-sur-Yvette Cedex, France
e-mail: edouard.audit@cea.fr
[3] Institut d'astrophysique spatiale, Université Paris-Sud, Bat. 121, 91405 Orsay, France.

Received 28 July 2006 / Accepted 13 December 2006

ABSTRACT

Aims. It is necessary to understand the dynamics of atomic gas to use complex modeling and to carry out detailed comparisons between theoretical models and observations.
Methods. In a companion paper, we present high resolution bidimensional numerical simulations of the interstellar atomic hydrogen. Here, we further characterize these simulations and we compare our results with various observations.
Results. We give statistics of the column density and velocity along the line of sight and show that they compare favorably with observations of high-latitude lines of sight. We compute synthetic HI spectra and qualitatively discuss the information that could be inferred if these spectra were observed. Finally, we extract CNM clouds and study their physical properties finding strong similarities with real clouds. In particular, we find that the clouds follow Larson-type relations, i.e. $M \propto L^{\gamma}$, where $\gamma \simeq 1.7$ (we propose a theory which predicts $\gamma \simeq 2.5$ in 3D) and $\sqrt{\langle \delta v^2 \rangle} \propto L^{0.4}$. We also find that the distribution, $\mathcal{N}(N)$, of the column density, N, of the CNM structures formed in the simulation follows $\mathcal{N}(N) \propto N^{-1.2}$ which is marginally compatible with the observational result obtained by Heiles & Troland (2005, ApJ, 624, 773). From the mass-size relation and the mass spectrum, we derive an exponent for the column density distribution close to the value obtained in the numerical simulation.
Conclusions. We conclude that the simulations reproduce various observational features reasonably well. An important implication suggested by our results is that the "turbulence" within the cold interstellar atomic gas is mainly the result of individual long living cloudlet (confined by an external warm medium) motions rather than supersonic turbulence within nearly isothermal clouds. Another important aspect is that the CNM structures produced in the simulation present various physical characteristics that are similar to the characteristics of the molecular clouds. This raises the question as to whether the physical properties of the molecular clouds are determined at a very early stage, before the gas becomes molecular.

Key words. hydrodynamics – instabilities – ISM: kinematics and dynamics – ISM: structure – ISM: clouds

1. Introduction

Since its first use in the 1950s (Ewen & Purcell 1951) the 21 cm transition of atomic hydrogen (HI) has been extensively used (e.g. Crovisier 1981; Kulkarni & Heiles 1987; Dickey & Lockman 1990; Joncas et al. 1992) to study the neutral atomic interstellar gas by numerous authors. Recent data have considerably improved our knowledge of this medium. Heiles & Troland (2003, 2005), using the Arecibo telescope, have done an extensive survey of HI clouds which has given reliable statistical results. To directly probe smaller scales of HI emission, various studies have been done using interferometers. Miville-Deschênes et al. (2003) and Taylor et al. (2003) use the Dominion Radio Astrophysical Observatory (DRAO) interferometer, Stil et al. (2006) use the Very Large Array (VLA) whereas McClure-Griffiths et al. (2005) use the Australian Telescope Compact Array (ATCA).

The observations of HI have revealed its complex multi-phase nature. In HI, cold and dense (CNM) structures are embedded in a warm (WNM) phase, with which they are approximately in pressure equilibrium, as predicted by detailed computations of thermal balance (Field et al. 1969; Wolfire et al. 1995, 2003). The observations have also revealed that this multi-phase medium is strongly turbulent making their interpretations even more challenging and indispensable the use of adapted numerical simulations.

Numerous numerical studies of the large scale ISM (e.g. Vázquez-Semadeni et al. 1995; Rosen & Bregman 1995; de Avillez & Breitschwerdt 2005a) and of the molecular clouds (e.g. MacLow & Klessen 2004) have been performed over the years and comparisons between observations and simulations have been carried out both for large scale simulations (e.g. Ballesteros-Paredes et al. 2002; de Avillez & Breitschwerdt 2005b) and for molecular clouds (Padoan et al. 2003; Ossenkopf & Mac Low 2002).

It is, however, only recently that numerical simulations devoted to the description of the warm and the dense atomic gas with a numerical resolution sufficient to describe the physical

scales of the problem (i.e. the CNM structures and the Field length) have been performed (Hennebelle & Pérault 1999, 2000; Koyama & Inutsuka 2000, 2002; Audit & Hennebelle 2005, hereafter Paper I; Heitsch et al. 2005, 2006; Vázquez-Semadeni et al. 2006). For this reason, no tight comparison between observations and theory has yet been carried out for HI at scales below 10 pc.

In a companion paper (Hennebelle & Audit 2007, here after Paper II), we present 2D high resolution numerical simulations aiming to describe self-consistently a turbulent atomic hydrogen flow from scales of few tens of parsec down to hundredth of parsec. The high resolution which is necessary to describe properly HI permits to obtain a good statistical description of the flow and to reach small scales close to the size of various small scale structures that have been observed in HI, like the so-called tiny small atomic structure (TSAS) and low column density clouds recently observed by Braun & Kanekar (2005) and Stanimirović & Heiles (2005). Therefore, in spite of the fact that these simulations are only bidimensional, they constitute a good starting point to carry out preliminary comparisons with the available HI data. Note that the dynamics of spatial scales which is covered by these simulations is about ten times larger than what can be done in 3D yet.

In this paper, we attempt to further characterize the results of the numerical simulations presented in Paper II and to perform comparisons between these simulations and the HI observations obtained in the Millennium Arecibo 21 centimeter absorption-line survey (Heiles & Troland 2003, 2005) since various interesting statistical informations have been extracted from these data. We also make a special effort to provide enough material to allow the observers to make easier the comparisons with their observations. In Sect. 2, we present some statistics of column density and velocity along the lines of sight since this information is the most direct observable. In Sect. 3, we present various examples of synthetic atomic hydrogen 21 cm line spectra in emission and absorption, showing in each case the corresponding density and velocity fields along the line of sight. We discuss the influence of the convolution by a Gaussian beam of various width on the synthetic spectra. Finally, we focus in Sect. 4 on the CNM structures formed in the simulations and their properties trying to make the link with some of the cloud properties available from the Millennium survey. Section 5 concludes the paper.

2. Lines of sight

In Paper II, the structure of the flow which results from the numerical simulation has been characterized by the probability distribution function of the density and pressure as well as by computing the velocity and density power-spectra and the energy spectrum. However, although very informative, these quantities are not easily obtained from the observations (and if so, would rely on various assumptions). On the other hand, column density and average velocity along the line of sight are more straightforwardly inferred from observational signals. Thus, we attempt here to further characterize the flow structure by giving some statistics of the column density and the velocity along the lines of sight. Since our experimental setup is strongly anisotropic (the flow enters from the left and right box faces and leaves from the top and bottom faces), we always show the results obtained along the x-axis and along the y-axis.

2.1. Line of sight characteristics

Top panel of Fig. 1 shows the column density, N, along the y-axis as a function of the x-coordinate (full line) as well as the column density along the x-axis as a function of the y-coordinate (dotted line). All the lines of sight available in the simulation, i.e. 10 000, are displayed. The average value is about 2×10^{20} cm^{-2}. These values are comparable to several values quoted in the literature for high latitude lines of sight (e.g. Heiles & Troland 2003) and indicate that the total amount of gas in the simulations is comparable to the total amount of gas along these lines of sight. We note, however, that only 20–30% of the lines of sight quoted by Heiles & Troland have such low column density. Our simulation is therefore representative of the most diffuse lines of sight.

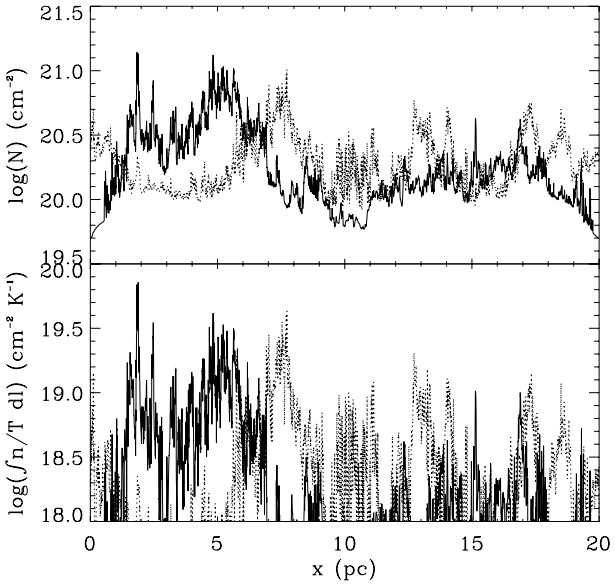

Fig. 1. *Top panel*: column density, N, along the lines of sight as a function of position. *Bottom panel*: integral of n/T along the line of sight. Full line represents lines of sight parallel to the y-axis, whereas dotted line represents lines of sight parallel to x-axis.

Bottom panel of Fig. 1 shows the integrated quantity $\int n/T \mathrm{d}l$ along x and y-axis. This quantity which traces mainly the CNM is directly obtained by HI 21cm line absorption spectra. An estimate of the CNM column density can be directly obtained by multiplying this quantity by the CNM temperature which is about 50 K. Again the values obtained are very similar to the values quoted by Heiles & Troland (2003) for the lines of sight having total HI column densities of about 2×10^{20} cm^{-2}.

Top panel of Fig. 2 shows the average velocity along the line of sight defined as:

$$\langle v_0 \rangle = \frac{\sum \rho v}{\sum \rho}, \tag{1}$$

whereas bottom panel of Fig. 2 shows the velocity dispersion along the line of sight:

$$\langle \delta v^2 \rangle = \frac{\sum \rho (v - v_0)^2}{\sum \rho}. \tag{2}$$

The mean velocity is close to zero (0.05 km s^{-1} for lines of sight parallel to y-axis and 0.39 km s^{-1} for lines of sight parallel to x-axis) although significant fluctuations (up to 2 km s^{-1}) are present, the standard deviation is 0.9 and 0.7 km s^{-1} for lines of sight parallel to y and x-axis, respectively. The velocity dispersion along the lines of sight is significantly larger. The mean value is about 2.29 and 2.5 km s^{-1} along y and x-axis respectively, whereas the standard variation is about 0.7 km s^{-1} in both cases. Interestingly, adopting a CNM sound speed of

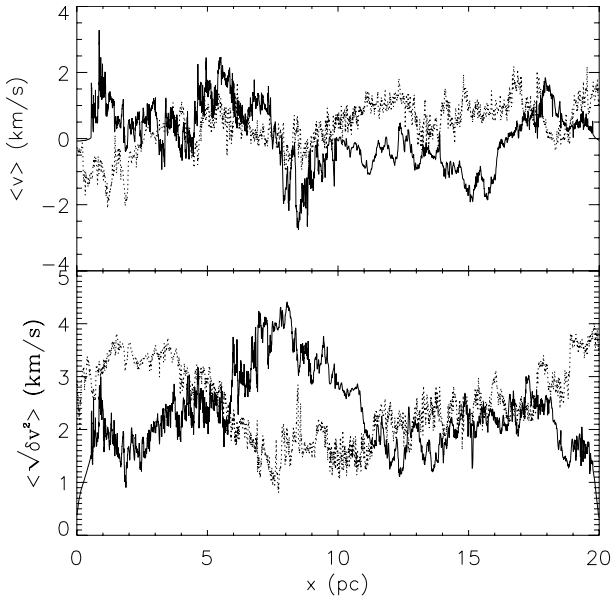

Fig. 2. *Top panel*: average velocity along the line of sight. *Bottom panel*: velocity dispersion along the line of sight. Full lines represent lines of sight parallel to y-axis whereas dotted lines represent lines of sight parallel to x-axis.

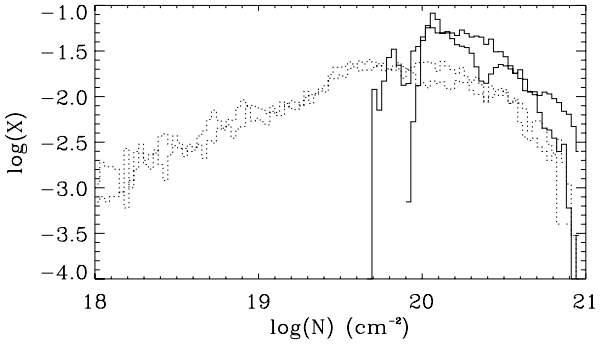

Fig. 3. Histogram of column density. The full lines represent the total column density along x and y-axis whereas the dotted lines represent the column density (along x and y-axis) of CNM only.

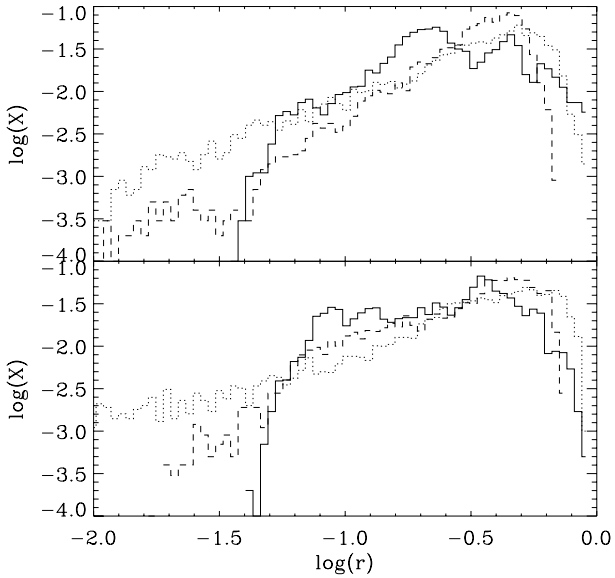

Fig. 4. Histogram of WNM (full line), CNM (dotted line) and thermally unstable gas (dashed line) column density fraction. *Top panel* is for lines of sight parallel to y-axis whereas *bottom panel* is for lines of sight parallel to x-axis.

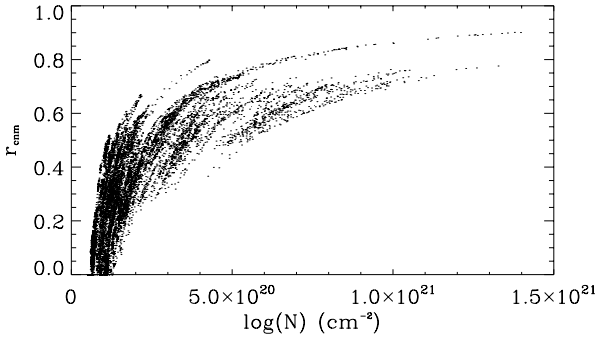

Fig. 5. Fraction of CNM column density as a function of total column density.

0.7 km s^{-1}, these values correspond to a Mach number of about $\mathcal{M}$ = 2.5 km s^{-1}/0.7 km s^{-1} $\simeq$ 3.5 which is similar to the values obtained for the CNM clouds by Crovisier (1981) and Heiles & Troland (2003).

2.2. Line of sight statistics

Here, we present statistics of lines of sight. Figure 3 displays the histogram of total column density along x and y-axis (full lines) and of CNM (defined as gas having temperature lower than 200 K) column density (dotted lines). Although our simulation described a coherent region of 20 pc, whereas the lines of sight of the Millennium survey are not correlated, it is worth doing some comparison with Fig. 7 of Heiles & Troland (2003). Their first panel shows that CNM column density peaks at $\simeq 1.5\times10^{20}$ cm^{-2} close to our case ($\simeq 1 \times 10^{20}$ cm^{-2}). We find that about 20% of lines of sight have a small ($<2 \times 10^{19}$ cm^{-2}) column density of CNM, whereas Heiles & Troland find about 30% of such lines of sight (first panel of their Fig. 7). They find that the total HI column density peaks at about 2×10^{20} cm^{-2}, which is close to what we find as well. They find no line of sight with column density smaller than $\simeq 1 \times 10^{20}$ cm^{-2}. In our case the smallest column density is about 7×10^{19} cm^{-2}. Note that the smallest column density of atomic gas observed in the Galaxy is about 4.5×10^{19} cm^{-2} (Lockman et al. 1986).

Figure 4 shows the histogram of the fraction, r of WNM (full lines), CNM (dotted lines), thermally unstable gas (dashed lines) along the lines of sight, e.g. $r_{\rm cnm} = n_{\rm c,cnm}/n_{\rm c,tot}$. Note the definition follows those of Paper I, i.e. WNM is gas having temperature higher than 5000 K whereas unstable gas has temperature between 200 and 5000 K. Top (bottom) panel is for line of sight parallel to y-axis (x-axis). The fraction of CNM can be compared with bottom panel of Fig. 7 from Heiles & Troland (2003). Again both appear to be similar. The median value in our case is about 0.34, whereas Heiles & Troland quote 0.3. We have about 10% of lines of sight for which the fraction of CNM is smaller than 0.05 and they find about 30% of lines of sight with no CNM. We have about 30% of lines of sight with a fraction of CNM larger than 0.5, whereas they find this fraction to be about 10%.

Figure 5 displays the fraction of CNM, $r_{\rm cnm}$, as a function of the total column density along the line of sight. It can be compared with Fig. 8 of Heiles & Troland (2003). A similar trend is observed in both cases, $r_{\rm cnm}$ increases with the total column density. However, the observations appear to have a dispersion larger than the simulation results. This could possibly be a

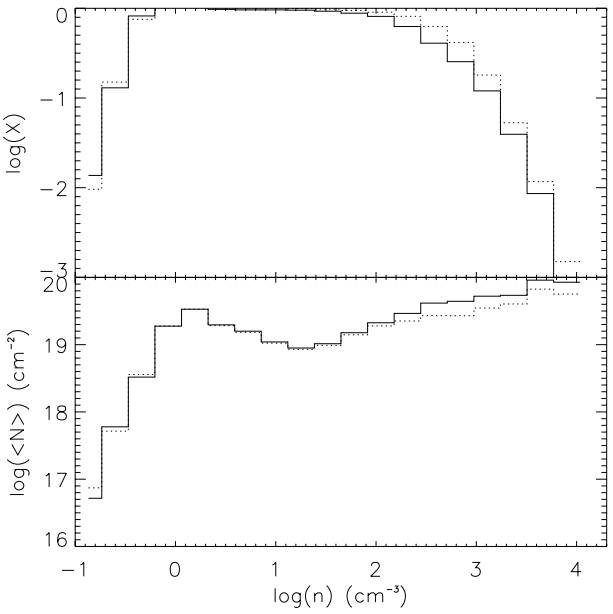

Fig. 6. Fraction of lines of sight which contain a gas particle of a given gas density (*upper panel*) and mean column density along the line of sight (*bottom panel*) of gas having a given density (only lines of sight which contain a fluid particle of the corresponding density are taken into account). Full lines represent lines of sight parallel to the y-axis whereas dotted lines represent lines of sight parallel to x-axis.

consequence of the fact that the observations probe several regions which are physically uncorrelated.

Altogether, these numbers appear to be similar. One should however keep in mind that our statistics are based on correlated lines of sight, whereas the lines of sight observed in the Millennium survey represent regions with a priori different physical conditions. As emphasized in Paper I, physical conditions like external triggering and level of turbulence do influence the physical parameters of the flow as the CNM/WNM fractions. Indeed, since the region that we are simulating is actively forming CNM structures, it is unsurprising that the number of lines of sight with no CNM is underestimated and the fraction of lines of sight dominated by CNM is overestimated. Nevertheless, the relatively good agreement suggests that the numerical setup we used leads to a reasonably realistic medium.

Another useful statistics is the number of lines of sight which cross a piece of fluid of a given density, n. The result is shown on top panel of Fig. 6 (logarithmic intervals of density are used). While most lines of sight intercept fluid particles of density between 0.5 and 100 cm^{-3}, there is about 10% lines of sight which cross gas denser than 1000 cm^{-3} and less than 0.1% which cross gas denser than 10^4 cm^{-3}. In particular, these results suggest that the so-called TSAS (Heiles 1997) are somehow rare events as suggested by Stanimirovíc et al. (2003) and Johnstone et al. (2003), even if quantitative prediction should be considered with great care.

Finally, an interesting question is: when a line of sight crosses a fluid particle of a given density, what is the mean column density of gas at this density along the line of sight? The result is shown in the second panel of Fig. 6 (note that we have plotted the mean column density of gas at density, ρ, such that $\log\rho_0 < \log\rho < \log\rho_0 + \mathrm{d}\log\rho_0$). While the mean column densities of gas at density 1–2 cm^{-3} and ≃100 cm^{-3} are approximately equal to about 3×10^{19} cm^{-2}, the mean column densities of gas denser than 10^3 cm^{-3} are about 2 to 3 times larger. This means that, although few lines of sight intercept fluid particles denser than 10^3 cm^{-3}, when it is the case, the column density of the dense gas is usually a significant fraction of the total column density along the line of sight.

3. HI spectra

3.1. Emission and absorption

Since HI spectra provide most of the available information on the interstellar atomic hydrogen, we give here various examples of synthetic HI spectra calculated from the numerical simulation, in emission and in absorption. This is certainly the most straightforward way of comparing observations and simulations. Figure 7 shows the density and the velocity fields along 4 lines of sight parallel to the x-axis (only half of the box simulation is displayed since the other half contains only WNM and no CNM structure) as well as the 21 cm line emission and extinction.

The first case (top panels) shows a line of sight with low density CNM structures (≃30 cm^{-3}). Two groups of clouds can be seen ($x \simeq 5.5$ and ≃6 pc), each of them being strongly substructured. The relative velocity of the two groups of clouds is about 5 km s^{-1} and each of them presents an internal velocity dispersion of a few km s^{-1}. In spite of this complexity, the emission spectrum appears to be relatively smooth. This is a consequence of the fact that the thermal broadening of the HI 21 cm line emission is not small compared to the turbulent broadening. The large component of width ≃20 km s^{-1} is the WNM emission. The two narrow components seen in emission and in absorption are due to the contribution of the two groups of clouds. The largest extinction is about 0.007 and the width of the lines is typically around 3–5 km s^{-1}. These numbers are very similar to the numbers quoted in Braun & Kanekar (2005) and Stanimirović & Heiles (2005).

The second case (second line of panels) shows a line of sight which contains four CNM structures of density higher than 100 cm^{-3}. Whereas three of them ($x \simeq 2.5$, $x \simeq 3.2$ and $x \simeq 5.5$ pc) present a modest velocity dispersion of few km s^{-1} with respect to the others, one of them (located at $x \simeq 5$ pc) moves at a velocity of about 4 km s^{-1} with respect to the other. As a consequence, the corresponding HI spectra present two peaks, the first one ($v \simeq 1$ km s^{-1}) being due to the contribution of the three structures moving at approximately the same velocities and the second ($v \simeq 4$ km s^{-1}) being due to the fourth structure ($x \simeq 5$ pc). Whereas the first peak is slightly broadened by the velocity dispersion of the 3 structures, the width of the second one is mainly thermal.

The third case shows about 10 CNM structures denser than 100 cm^{-3} and about the same number of CNM structures having a lower density. A velocity gradient of about 1 km s^{-1}/pc takes place between $x \simeq 1$ and $x \simeq 6$ pc. As a consequence, the HI spectra present a single peak, instead of 2 in the preceding cases, which is significantly broadened by the velocity dispersion of the structures. Note that this spectrum is qualitatively similar (temperature, extinction and shape) to the spectra shown by Heiles (2001) except for the width which is 2 times larger than the case presented here.

The fourth case shows a line of sight which crosses the highest density reached in Fig. 1 of Paper II ($x \simeq 1.65$ pc and $y \simeq 7.07$ pc). The HI 21 cm line is strongly saturated because of the large column density. The spectra are again broadened by the velocity dispersion between CNM structures. Again, the complex structure of the flow cannot be easily recovered from the HI spectra which are relatively smooth.

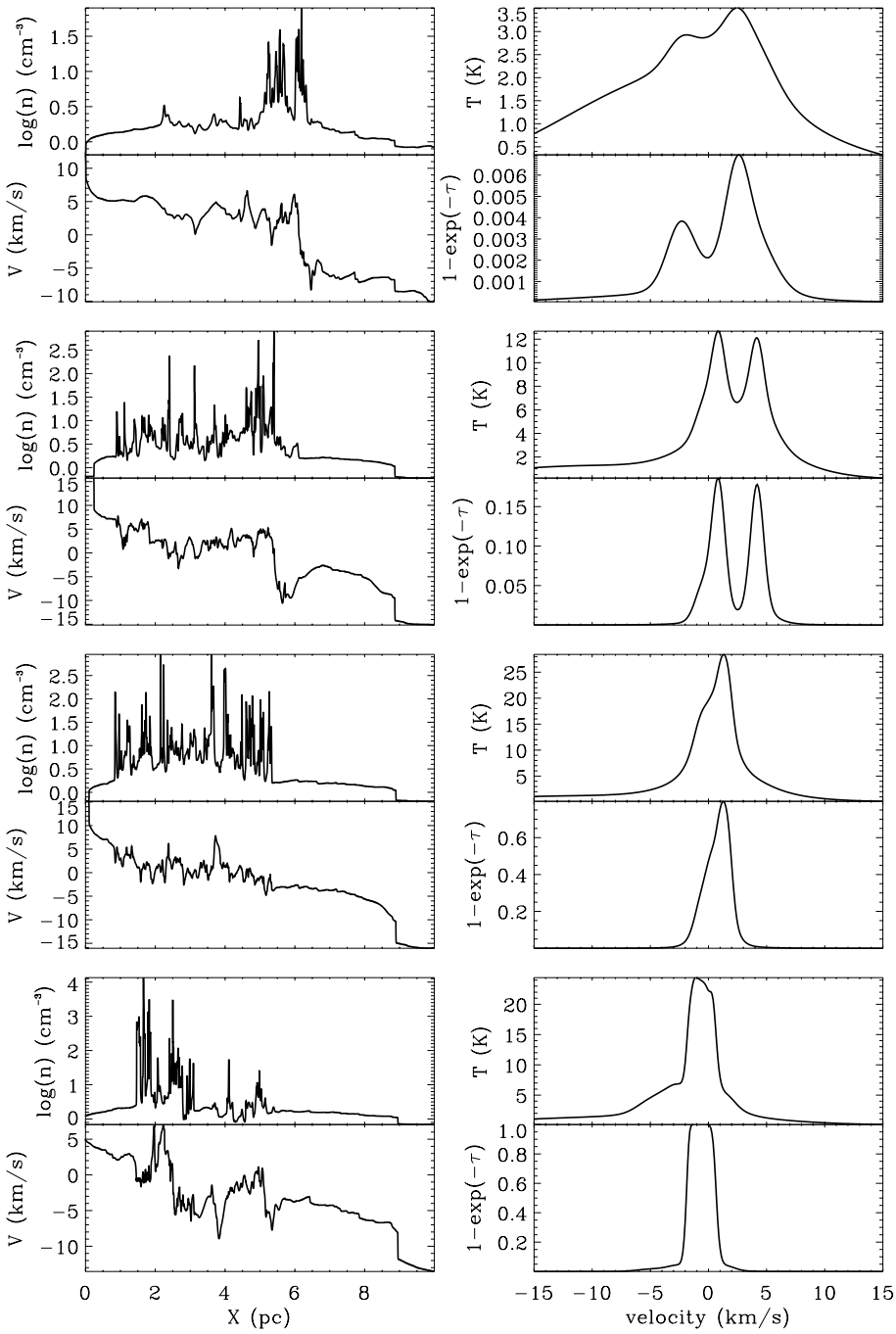

Fig. 7. Density and velocity fields along 4 lines of sight (parallel to x-axis) and synthetic HI spectra in emission and in absorption calculated along these lines of sight.

Figure 8 shows four lines of sight along the y-axis. Indeed, since our experimental setup is strongly anisotropic, it is worth to see what are the consequences of this anisotropy on the synthetic HI spectra. In particular, along the y-axis few uncorrelated groups of structures can contribute to the synthetic signals. This is well illustrated by the first, second and third cases in which 3 to 5 groups of structures are present. Each group presents an internal velocity dispersion of a few km s^{-1} and an average velocity with respect to the other groups which can be as high as $\simeq$5 km s^{-1}. Interestingly, this is somehow similar to the structures obtained by Hennebelle & Passot (2006) in the case where significant Alfvén waves are initially present in the flow. Whereas in their case, this was due to the effect of Alfvén waves which tend to subfragment the CNM structures, here the subfragmentation of the group of structures is likely due to the turbulent fluctuations. As a consequence, the synthetic spectra are on average broader than the spectra obtained along the x-axis (factor $\simeq$1.3−1.5).

The fourth case (Fig. 8) corresponds to the line of sight parallel to the y-axis which crosses the highest density reached in the simulation. As for the fourth case (Fig. 7), the 21 cm line is strongly saturated. The narrow peak seen in emission is produced by the strong density fluctuation (located at $x \simeq 7$ pc) which is also displayed in Fig. 5 of Paper II. As explained in Paper II, we believe that this structure is a good candidate to explain the TSAS observed in the atomic gas. This spectrum could therefore constitute a typical signature of such event. Note that in the fourth case of Fig. 7, this narrow component is not seen because in front of it, stands a less dense structure ($\simeq 10^3$ cm^{-3}) which has a high extinction. On the contrary, in the present case, there is no dense structure on the right side of the densest peak.

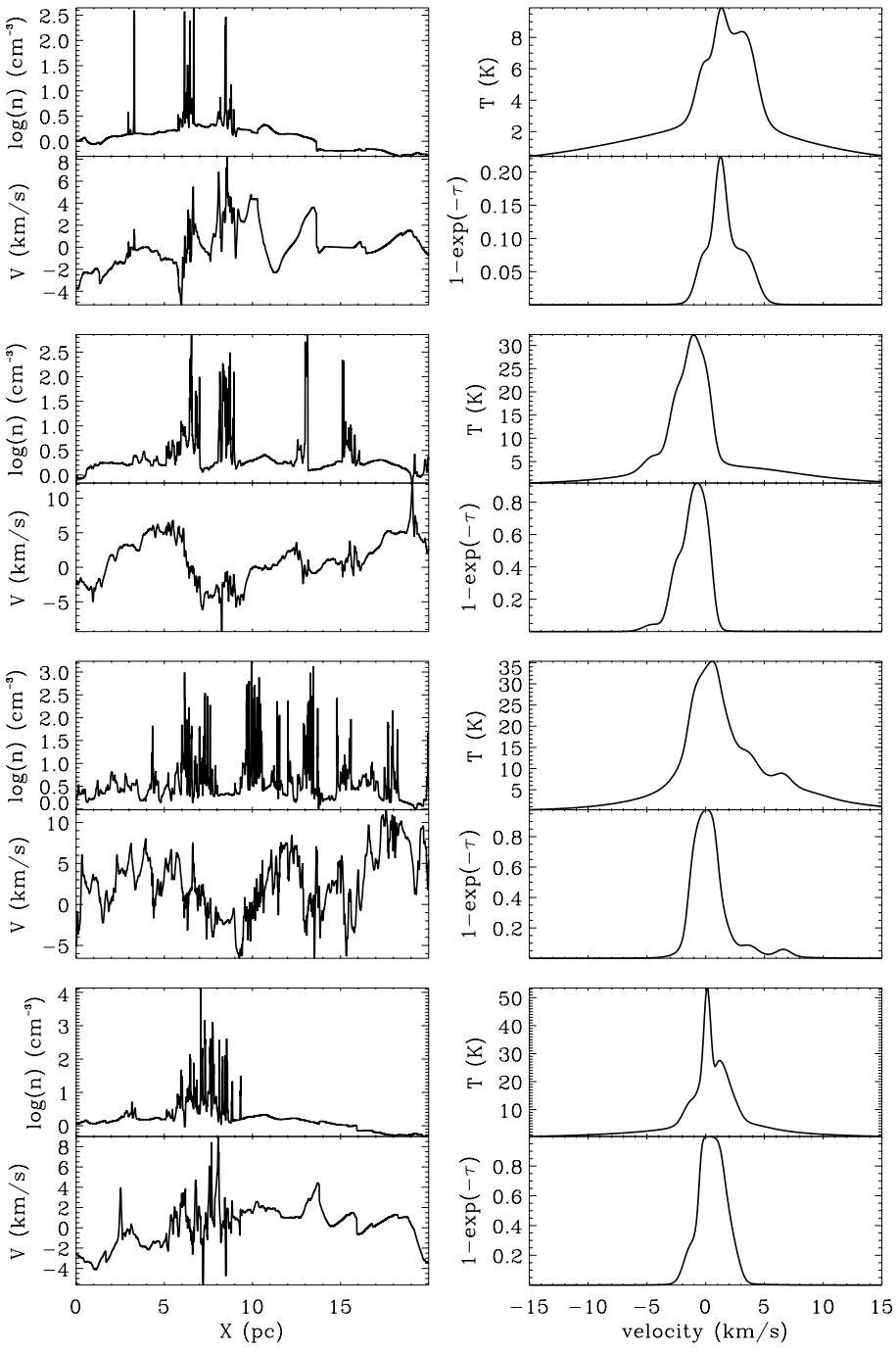

Fig. 8. Density and velocity fields along 4 lines of sight (parallel to y-axis) and synthetic HI spectra in emission and in absorption calculated along these lines of sight.

3.2. Effect of finite resolution

Here, we investigate the effect of finite resolution on the HI emission spectra. We convolve the HI spectra calculated along the lines of sight by Gaussian functions of various widths at half maximum, b. Figure 9 shows the results. Four series of spectra showing the influence of a finite resolution are displayed. The full line of first panel of each series shows the same spectra as those shown in Fig. 8, (left-top series of spectra is first case of Fig. 8, left-bottom is second case, right-top is third case, whereas left-bottom is fourth case). The full line of second, third and fourth panels of each series shows the spectra obtained by convolving the spectrum distribution by a Gaussian function of width at half maximum equal to b = 10, 20 and 40 cells respectively. The dotted (dashed) lines of each panel show the unsmoothed spectra shifted from the central position by Δ = −5(5), –10 (10), –20 (20) and –40 (40) cells respectively.

Left-top series (first case of Fig. 8) show that there is a significant variability of the HI 21 cm emission spectra when different lines of sight are selected (dotted and dashed lines). This has severe consequences on the convolved spectra which vary significantly when the width at half maximum of the Gaussian function used for the convolution, increases. As can be seen, the shape of the unconvolved spectra (first panel) is rather different from the shape obtained with b = 10, 20 and 40.

Left-bottom series (second case of Fig. 8) and right-top series (third case of Fig. 8) show cases for which the variability of the spectra is much less important than in the previous case. The general shape of the convolved spectra (full lines) does not change much, the fluctuations appear to be on average smaller

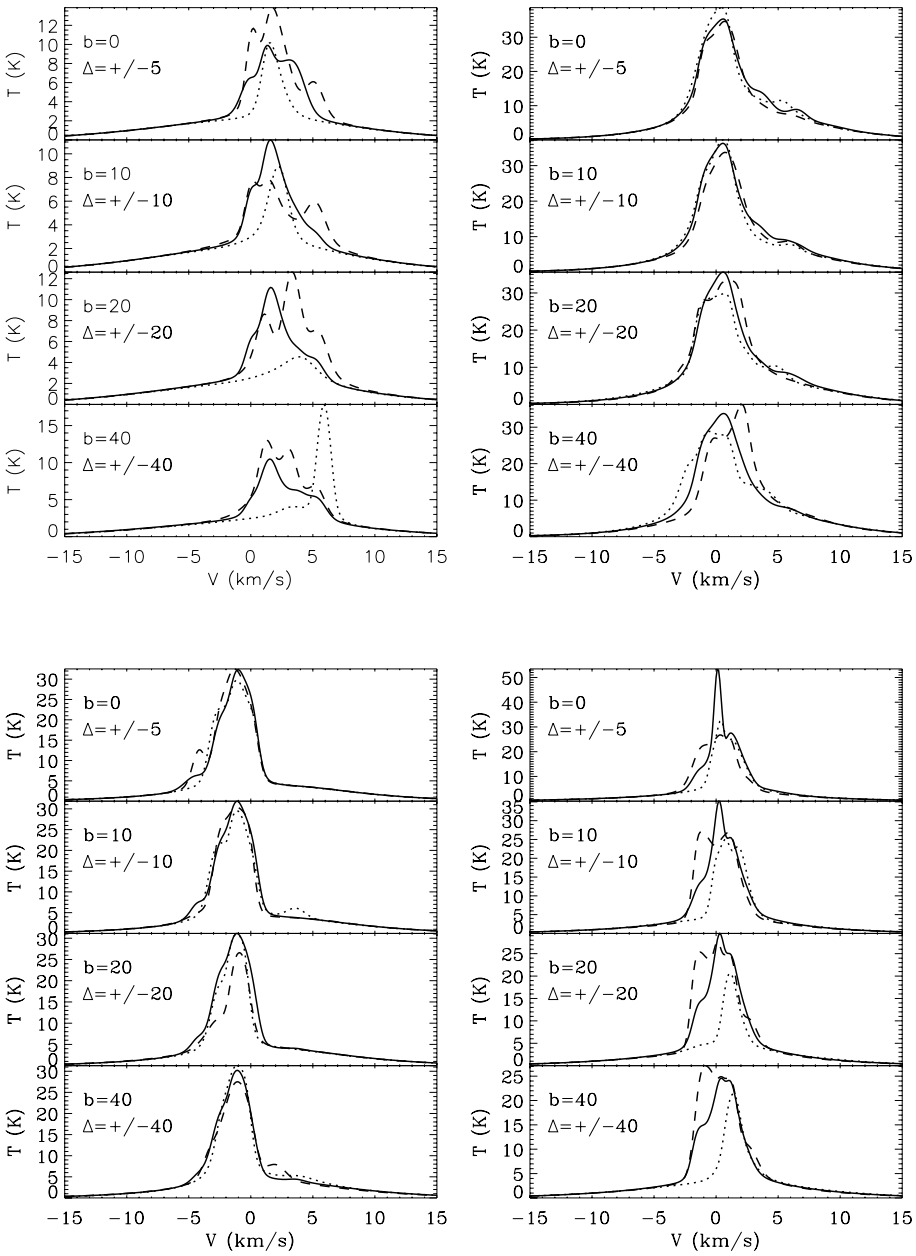

Fig. 9. Four series of spectra showing the influence of a finite observational spatial resolution. The full line of *first panel* of each series show the same spectra than those shown in Fig. 8, the full lines of *second*, *third* and *fourth panels* show the spectra obtained by convolving the spectrum distribution by a Gaussian of width at half maximum equal to respectively b = 10, 20 and 40 cells. The dotted (dashed) lines of each panel show the unsmoothed spectra shifted from the central position by Δ = −5 (5), –10 (10), –20 (20) and –40 (40) cells respectively.

than ≃10% with some stronger fluctuations of about ≃20−30%. The difference between this behaviour and what has been found in the previous case, is largely due to the fact that the CNM structures are much smaller in the latter than in the former. Therefore the spatial length over which the column density varies significantly, is also smaller in left-top case than in these 2 cases, making the dependency on the lobe effect more important.

Right-bottom series (fourth case of Fig. 8) show also significant variability in spite of the large emission value. This is due to the fact that the line of sight (Δ = 0) crosses a small scale and dense structure (seen in Fig. 5 of Paper II) which results from a strong collision between 2 CNM structures. Therefore, as indicated in Fig. 6, the column density varies significantly along the line of sight in few cells.

On average, the smoothed spectra are not much broader than the unsmoothed one. This is certainly a consequence of the fact that the velocity dispersion along the lines of sight presents variations which are smaller than its average value (Sect. 2.1).

4. Clouds properties

In Paper II, the mass spectrum of the structures formed in the simulation has been measured and theoretical arguments to explain it, have been presented. Here, we further study the structures properties. First, we consider the case of structures simply defined by the clipping procedure explained in Papers I and II. Second in order to quantify the fact that the structures are spatially correlated and not randomly distributed, we investigate some properties of groups of structures.

4.1. Properties of individual clouds

We study various structure properties which could be compared with observations or with other theoretical works. We pay special attention to the distribution of column density within clouds, since an interesting observational result has been obtained by Heiles & Troland (2005) with which comparison is possible.

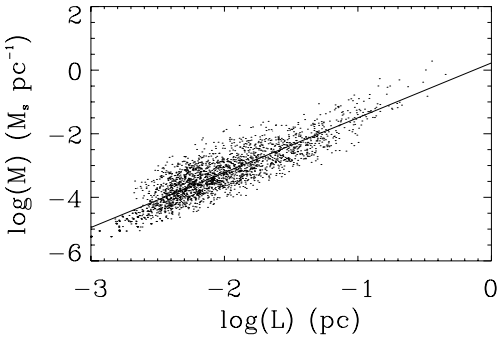

Fig. 10. Mass of the structures as a function of their size. One finds the relation $M \propto L^{\gamma}$ with $\gamma \simeq 1.7$.

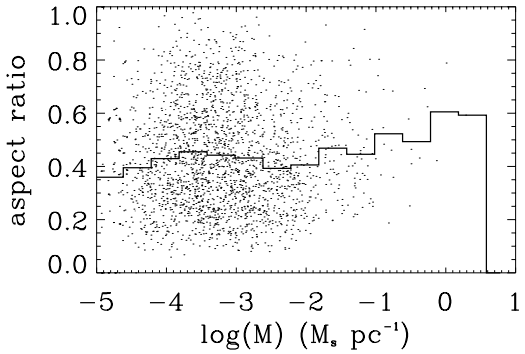

Fig. 11. Aspect ratio of the clouds as a function of their mass. The solid line shows the average value per logarithmic interval of mass.

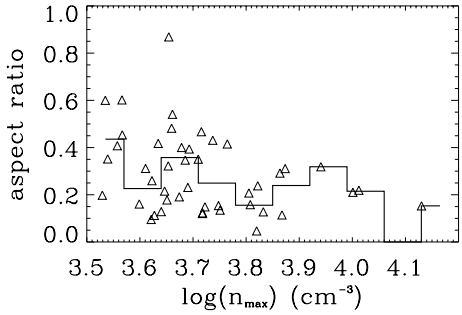

Fig. 12. Aspect ratio of the densest regions as a function of the largest gas density within the region. The solid line shows the average value per density interval.

In the following, we define the cloud size, L, as $L = \sqrt{I_1/M}$, where M is the cloud mass whereas I_1 is the highest inertial momentum (I_2 being the smallest), i.e. the highest eigenvalue of the inertial matrix, $\mathcal{I}$, defined as $\mathcal{I}_{xx} = \int y^2 \mathrm{d}m$, $\mathcal{I}_{yy} = \int x^2 \mathrm{d}m$ and $\mathcal{I}_{xy} = \mathcal{I}_{yx} = -\int xy \mathrm{d}m$.

4.1.1. Mass-size relation and size distribution

An interesting property for cloud characterization is the mass-size relation. Figure 10 shows the mass of the structure as a function of their size. A clear correlation is seen, leading to the relation $M \propto L^{\gamma}$ with $\gamma \simeq 1.7$.

Since, as will be seen below, this relation turns out to be useful to understand the column density distribution, it is worth to understand its physical origin. For this purpose, we consider the distribution function, $\mathcal{N}(L)$, of structures of size L. The number of structures of size between L and $L + \mathrm{d}L$ is equal to the number of structures of mass between M and $M + \mathrm{d}M$, $\mathcal{N}(L)\mathrm{d}L = \mathcal{N}(M)\mathrm{d}M$ where $M \propto L^{\gamma}$. In Paper II, we obtain that $\mathcal{N}(M) \propto M^{-\beta}$ with $\beta \simeq 1.7$. Therefore, we have: $\mathcal{N}(L) = \mathcal{N}(M)\,\mathrm{d}M/\mathrm{d}L \propto L^{-\beta\gamma+\gamma-1}$. With the values of β and γ given above, we have: $-\beta\gamma + \gamma - 1 \simeq -2.19$. This implies that $\mathcal{N}(L)L^2 \simeq L^{-0.19}$, i.e. the number of structures of a given scale L within a (bidimensional) volume aL^2, where a is a constant larger than 1, is almost the same as the number of structures of scale L' within a volume aL'^2. This implies that the flow is nearly scale-invariant (see Elmegreen 1997; Padoan & Nordlund 2002). This is likely a consequence of the flow being turbulent, although in the present problem, there are characteristic scales which may explain the deviation from the scale-invariant behaviour. Note that it is also possible that the size of the simulation is still insufficient and that the discrepency from $\mathcal{N}(L) \propto L^{-2}$ is due to the influence of the numerical mesh or the injection scale.

4.1.2. Cloud shape

Figure 11 shows the aspect ratio of the cloud defined as $\sqrt{I_2/I_1}$. The solid line represents the mean value per logarithmic mass interval. The mean aspect ratio is approximately constant and equal to about 0.4 until $M \simeq 0.1\ M_s$/pc. It then increases to about 0.6 for larger mass. Nevertheless, we note that there is a considerable dispersion, some structures being very elongated.

Another related question is the shape of the very dense regions observed in the simulations (see Sect. 3.2 of Paper II). Since this high density component is created by shocks, it is expected that these regions should be very elongated. Figure 12 shows the aspect ratio of these regions as a function of the peak density (note that since these regions are rare, 6 time steps have been used to provide this plot) and confirms that these structures are elongated with a mean aspect ratio of about ≃0.3. We note that a significant fraction of them has an aspect ratio smaller than 0.2, which is significantly smaller than the mean aspect ratio of unshocked CNM structures. Indeed very few CNM clouds have an aspect ratio smaller than 0.2. This suggests that this could constitute an interesting test for the assumption of TSAS being shocked CNM structures.

4.2. Column density distribution of clouds

In the quest for comparison between observations and simulations, an interesting result obtained by Heiles & Troland (2005), appears to deserve special attention. Heiles & Troland show that the column density distribution of their CNM structures follows the relation $\mathcal{N}(N) \propto 1/N$. In this section, we study in some details the column density distribution of the CNM structures and propose a theoretical explanation for this relation.

4.2.1. Numerical results

Here, we display the column density distribution, $\mathcal{N}(N)$ obtained by putting together the column density distribution of all the structures identified in our simulation. The result is shown in Fig. 13 which shows the number of lines of sight, n_l, per logarithmic interval of column density, $\mathrm{d}n_l/\mathrm{dlog}N = N\mathrm{d}n_l/\mathrm{d}N = N\mathcal{N}(N)$, for various numerical resolutions.

The low column density part is obviously spoiled by numerical resolution effects. In the intermediate part, say between 3×10^{18} cm^{-2} and $\simeq 3 \times 10^{19}$ cm^{-2}, the distribution does not appear to depend on the numerical resolution for $l_g > 5000$. This suggests that, in this range of column density, numerical

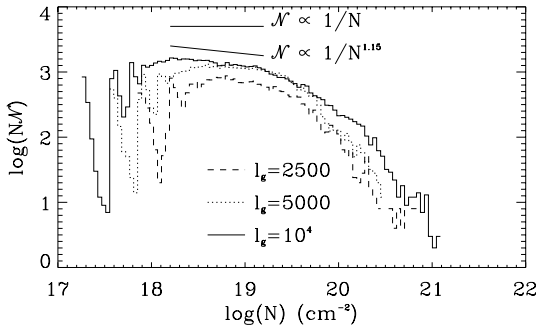

Fig. 13. Number of lines of sight (crossing a single CNM structure) per logarithmic column density interval. Full line corresponds to the $(10^4)^2$ cells simulation, dotted line is for the $(5000)^2$ one, dashed line is for the $(2500)^2$ cells simulation.

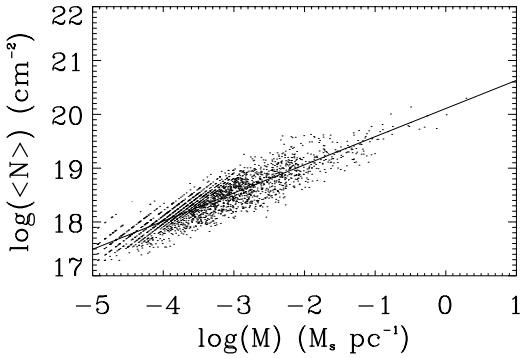

Fig. 14. Average column density of the structures as a function of their mass. One finds the relation $\langle N \rangle \propto M^{\eta}$ with $\eta \simeq 0.52$.

convergence has been reached. On the contrary, the high column density part strongly depends on the numerical resolution. In particular, the higher the resolution, the larger the number of lines of sight having high column density. We therefore believe that only the intermediate column density part is physically significant.

As can be seen from the highest resolution simulation (solid line) displayed in Fig. 13, the column density distribution is stiffer between 1.5×10^{19} and 3×10^{19} cm^{-2} than between 1.5×10^{18} and 1.5×10^{19} cm^{-2}. Since there is no clear physical reason for this to be true, this is most likely a numerical effect due to the finite size of our numerical experiment. Since the size of the simulation box is only 20 pc and the WNM density about 0.8 cm^{-3}, it is indeed difficult to produce structures with column density equal to, or higher, than about $20 \times 3.08 \times 10^{18} \times 0.8 \simeq 5 \times 10^{19}$ cm^{-2}. Therefore one expects that the number of big structures and therefore the number of lines of sight with large column density drop above a certain threshold. The value of this threshold for the column density is certainly smaller than $\simeq 5 \times 10^{19}$ cm^{-2}. This is in good agreement with what has been found in Paper II for the mass spectrum (Fig. 15) which presents a cutoff for high mass as well.

Therefore, we believe that the most reliable part of the column density distribution is the one between $\simeq 1.5 \times 10^{18}$ and 1.5×10^{19} cm^{-2}. Note that this range of column density corresponds to the part of the mass distribution, (Figs. 15–18 of Paper II) for which numerical convergence has been reached. The solid line shows that between 1.5×10^{18} and 1.5×10^{19} cm^{-2}, one has about $\mathcal{N}(N) \propto 1/N^{1.15} \simeq 1/N^{1.2}$ which is slightly stiffer but nevertheless close to the $\mathcal{N}(N) \propto 1/N$ distribution. Although the disagreement appears to be statistically significant (Heiles 2006, Private Communication), it appears to be mainly due to the column densities larger than 10^{20} cm^{-2}, which we cannot probe here. It is also possible that the observational column density distribution is biased because of large column density components being blends of two smaller components or because of small column density being missed (Heiles 2006, Private Communication). Note that indeed, Heiles & Troland (2005) infer $\mathcal{N}(N) \propto 1/N$ for N between 2×10^{18} and 2×10^{20} cm^{-2}. Future studies using larger box size and larger numerical resolution are required to investigate whether $\mathcal{N}(N) \propto 1/N$ still occurs between 2×10^{19} and 2×10^{20} cm^{-2}.

4.2.2. Physical explanation

Here, we propose a physical explanation for the column density distribution being proportional to $\mathcal{N}(N) \propto N^{-\alpha}$, with $\alpha \simeq 1-1.2$.

For this purpose, we make the assumption that the clouds are sufficiently uniform for us to consider that the column density within the cloud does not strongly fluctuate. Figure 14 displays the mean structure column density as a function of their mass, M. A very good agreement is obtained with the relation $\langle N \rangle \propto M^{0.5}$.

This result can be understood as follows. Let us consider a spherical CNM cloud of uniform density n. Its mass can be written $M \simeq nL^2$ and the column density $N \simeq nL$. Thus $\langle N \rangle \propto M^{\eta}$ with $\eta = 0.5$. In the case we are considering, $M \propto L^{\gamma}$ which implies that the CNM structures are not spherical clouds with uniform density. To fix idea, we consider 2 cases.

First, the CNM clouds are roughly roundish but the density is not uniform because the internal structure is complex. The number of lines of sight crossing the structure is proportional to L, thus the mean column density follows $\langle N \rangle \propto L^{\gamma-1} \propto M^{(\gamma-1)/\gamma}$. With $\gamma = 1.7$, we have $(\gamma - 1)/\gamma \simeq 0.41$.

Second, the CNM clouds are filaments with uniform density. The major axis has a length L, whereas the minor axis has a length $L^{\gamma-1}$. If the filament is seen along the minor axis, the mean column density again follows $\langle N \rangle \propto L^{\gamma-1} \propto M^{(\gamma-1)/\gamma}$. If the filament is seen along the major axis, then $\langle N \rangle \propto L \propto M^{1/\gamma}$ with $1/\gamma \simeq 0.59$.

Since all the values found are slightly above or slightly below 0.5, it is not surprising to find $\eta \simeq 0.5$.

The number of lines of sight crossing a structure of column density between N and $N + \mathrm{d}N$ is proportional to the number of structures having a mass between M and $M + \mathrm{d}M$ times the length of the structures (since the number of line of sight crossing a structure of size L is proportional to L). Thus we have: $\mathcal{N}(N)\mathrm{d}N \propto \mathcal{N}(M) \times M^{1/\gamma} \times \mathrm{d}M$. This leads to $\mathcal{N}(N) \simeq N^{(-\beta+1/\gamma+1-\eta)/\eta}$. Since with $\beta = 1.7$, $\gamma = 1.7$ and $\eta = 0.5$ we have $-(-\beta + 1/\gamma + 1 - \eta)/\eta \simeq 1.22$, we get: $\mathcal{N}(N) \propto 1/N^{1.22}$. This value is remarkably close to what is measured in the simulation.

The good agreement between the analytical value and the exponent measured in the simulation, suggests the validity of the approach. However, since we used the value γ, inferred from the simulation, it could be that its value is different in the ISM (as previously discussed, the size of the computational box or the numerical resolution could be insufficient). In particular, it could be, that real atomic flows are closer from strict scale invariance than what has been found in the simulation. If instead of taking the value of γ measured in the simulation, we assume $\mathcal{N}(L) \propto L^{-2}$, thus $L^{-2}\mathrm{d}L = M^{-\beta}\mathrm{d}M$ which leads to $M \propto L^{\gamma}$, $\gamma = 1/(\beta - 1)$. With this value of γ, we have $-(-\beta + 1/\gamma + 1 - \eta)/\eta = 1$ which is exactly the value inferred by Heiles & Troland (2005). Interestingly, the result appears to be independent of β and η.

Let us stress that the result, $\mathcal{N}(N) \propto N^{-\alpha}$, with $\alpha \simeq 1-1.2$, is largely a consequence of $\mathcal{N}(L) \propto L^{-2}$ and of the fact that the

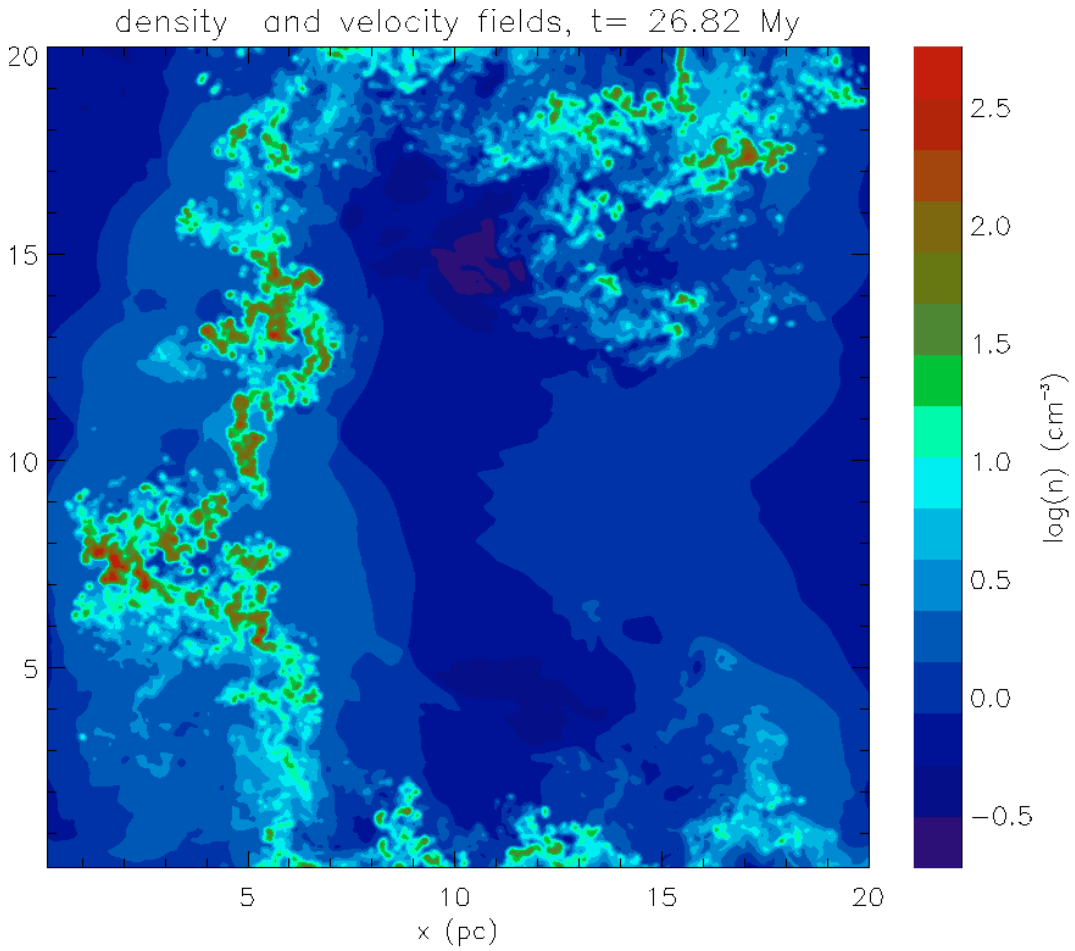

Fig. 15. Smoothed density field. The original density field has been convolved with a Gaussian having a width at half maximum equal to $b = 40$ cells leading to a spatial resolution of about 0.1 pc.

column density across a structure is nearly proportional to its size, which is due to the thermally bistable nature of the flow, since in that case, the density is determined almost entirely by the mean pressure and does not depend on scale or mass. Future works, using larger simulations, may clarify to which extent such flow follows $\mathcal{N}(L) \propto L^{-2}$.

4.2.3. The 3D case

Since the simulation and the theoretical derivation are bidimensional, it is worth investigating the value of the exponent of the column density distribution in the 3D case. The theory developed in Paper II for the structure mass spectrum, $\mathcal{N}(M)$, predicts that $\mathcal{N}(M) \propto M^{-\beta}$ with $\beta \simeq 16/9$. Assuming scale invariance, we get $\mathcal{N}(L) \propto 1/L^3$, which leads to: $L^{-3}\mathrm{d}L = M^{-\beta}\mathrm{d}M$ and thus to $M \propto L^{\gamma}$, with $\gamma = 2/(\beta - 1)$. We again make the assumption that $\langle N \rangle \propto M^{\eta}$. For a spheroidal cloud with uniform density, we have obviously $\eta = 1/3$. In 3D, we have $\mathcal{N}(N)\mathrm{d}N = \mathcal{N}(M) \times L^2 \times \mathrm{d}M$. Thus we obtain $\mathcal{N}(N) \simeq N^{(-\beta+2/\gamma+1-\eta)/\eta} = N^{-1}$, which is again the value inferred by Heiles & Troland (2005) (as in the 2D case, it does not depend on β or on η).

Note that for $\beta = 1.8$, we get $\gamma = 2/0.8 = 2.5$, implying $M \propto L^{2.5}$. This is very similar to the mass-size relation inferred by Larson (1981) for the molecular clouds. Even more interesting is the comparison with the results obtained by Heithausen et al. (1998) for CO clumps of mass ranging from 10^4 solar mass down to Jupiter mass. For these clouds, they measure $M \propto L^{2.3}$, $\mathcal{N}(M) \propto M^{-1.8}$ and $\mathcal{N}(L) \propto L^{-3}$. This is consistent with what we infer for the CNM clouds.

4.3. Group of structures properties

The aim of this section is to further characterize the structure of the flow and in particular the fact that the CNM structures appear to be highly correlated and not randomly distributed.

4.3.1. Methods

In order to achieve this, we smooth the density field by convolving it with Gaussian of various widths at half maximum, b. This has the advantage of mimicking observations done with a telescope having a Gaussian lobe and a spatial resolution equal to $b \times \mathrm{d}x$, where $\mathrm{d}x$ is the size of one of our cells. For $b = 40$, this leads to a resolution of about 0.08 pc. At 100 pc of distance, this corresponds to a resolution of 3 arcmin which is comparable to the resolution of the Arecibo telescope. Figure 15 shows the density field displayed in Fig. 1 of Paper II which has been convolved by a Gaussian of width at half maximum equal to $b = 40$ cells. As expected, the field displayed in Fig. 15 is more uniform than the field displayed in Fig. 1 of Paper II, although significant large scale fluctuations persist. As in Paper II, we identify the structures by applying a simple clipping algorithm, i.e. the structures are defined as groups of connex cells denser than a density threshold ρ_0. Two values of ρ_0 are considered in the following, namely 5 and 30 cm^{-3}.

We stress that the analysis presented in this section, ought to characterize an *ensemble* of individual, disconnected from each other, CNM structures which are spatially correlated and would

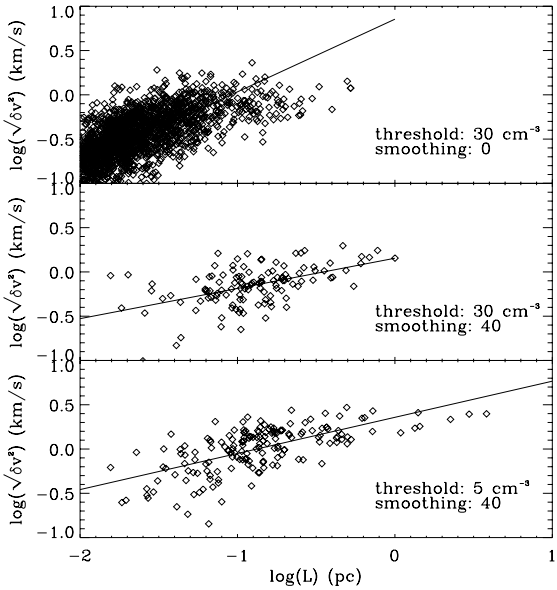

Fig. 16. Measure of the internal velocity dispersion of structures extracted from numerical data obtained with different smoothing and clipping thresholds.

be seen with a telescope of insufficient spatial resolution as a coherent cloud.

4.3.2. Velocity dispersion

The cloud velocity dispersion is an interesting parameter for the understanding and the characterization of the turbulence which takes place within the atomic medium. Before we pursue, we would like to stress that the use of the word *turbulence* in referring to the gas motions should be made with some care. Indeed, the structure of the flow studied here is very different from the incompressible fluids which have been extensively studied and which constitute our basic conception of the turbulent processes. As discussed above, the turbulence is produced by individual cloudlets motion rather than by eddies in a nearly homogeneous medium. In particular, the coupling between the various spatial scales is presumably strongly modified by the stiff density fronts.

The cloud velocity dispersion is defined as stated by Eq. (2), where v_0 is the mean cloud velocity and where all cells having a density above the threshold and lying in the area defined by the smoothed density field have been counted (we stress that we use unsmoothed data to compute the velocity dispersion). Figure 16 shows results for $b = 0$ and 40 and clipping thresholds 5 and 30 cm^{-3}.

In the case with no smoothing, we find that most of the structures have a velocity dispersion lower than 1 km s^{-1} meaning that most of structures have a subsonic velocity dispersion. By performing a simple linear fit, we infer: $\sqrt{\delta v^2} \simeq 7$ km s^{-1} $\times$ $(r/1\ \mathrm{pc})^{0.8}$. Note that the size of structures found with no smoothing is generally smaller than 0.1 pc so that this relation is valid only up to $\sqrt{\delta v^2} \lesssim 1$ km s^{-1}.

With $b = 40$, the structures are bigger and the velocity dispersion higher. As can be seen, it is not strongly affected by the clipping threshold (factor $\simeq$2). Typical velocity dispersions are now around 1 km s^{-1} and up to 3 km s^{-1} for the biggest structures. We infer $\sqrt{\delta v^2} \simeq 1.4$ km s^{-1} $\times(r/1\ \mathrm{pc})^{0.34}$ for a clipping threshold of 30 cm^{-3} and $\sqrt{\delta v^2} \simeq 2.2$ km s^{-1} $\times(r/1\ \mathrm{pc})^{0.4}$ for a clipping threshold of 5 cm^{-3}. We note that these values are reminiscent of the values observed in HI clouds by Crovisier et al. (1981) and Heiles & Troland (2003, 2005), although Fig. 12 of Heiles & Troland (2003) suggests that the mean value of the Mach number inside structures is about 3. In our case, it is slightly lower, 1.5–2.5, depending on the threshold which is used to define the structures. At this stage, it seems difficult to do a more quantitative comparison since the present simulations are only 2D. In particular, the approach used in this section, excludes any projection effect along the line of sight.

The fact that the internal velocity dispersion of CNM structures is low (<1 km s^{-1}) but that the velocity dispersion of the groups of structures is comparable to observations, suggests that the turbulence inside CNM clouds is largely due to individual long-living cloudlet motions.

Again, we note that the velocity dispersion-size relation is reminiscent of what is observed in the case of molecular clouds (Larson 1981).

4.3.3. Filling factor

One of the striking aspects of the structures displayed in Fig. 1 and 2 of Paper II is that the CNM appears to be very fragmented even in the densest parts of the flow. In order to quantify this effect, we have computed the filling factor of the structures extracted from the smoothed data. This is obtained by simply computing within these structures, the filling factor of the gas (taken from unsmoothed data) having a density above the clipping threshold. The result is displayed in Fig. 17 which shows the filling factor for various b and clipping thresholds. As expected, the value of the filling factor presents a significant scatter and depends on b, the width at half maximum of the Gaussian used to compute the smoothing. Typical values range nevertheless between 0.8 and 0.2 whereas the average value is about $\simeq$0.5.

5. Conclusion

In a companion paper, high resolution numerical simulations of the turbulent interstellar atomic hydrogen have been presented. Because of the high spatial resolution (0.002 pc) reached in these simulations, scales approaching the size of the smallest structures observed in HI can be described.

In this paper, we have further analyzed these numerical data in order to make preliminary comparisons with HI observations. We provide statistical informations on column density, average velocity and velocity fluctuations along the line of sight and, when possible, we compare with the results of the Millennium Arecibo 21 centimeter absorption line carried out by Heiles & Troland (2003, 2005).

We compute HI 21 cm line spectra in emission and in absorption along eight lines of sight. We reach the conclusion that although these spectra are relatively smoothed the lines of sight from which they are calculated appear to be highly complex and fragmented. In particular, the "turbulence" is produced by the individual motions of few long living CNM structures rather than by motions within nearly homogeneous or isothermal medium. This suggests that the Mach number deduced from observation is more indicative of the velocity dispersion from cloud to cloud rather than of the internal velocity dispersion of the clouds. We also consider the influence of a Gaussian lobe on the HI spectra and find that, it has in some cases, a drastic influence.

To further characterize the CNM structures produced in the simulation, we have studied some of their properties, namely mass-size relation and shape. In an attempt to describe the high

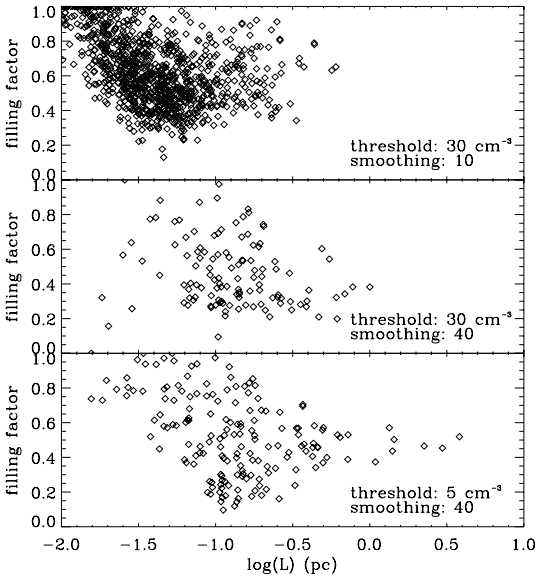

Fig. 17. Measure of the cloud filling factor in structures extracted from numerical data obtained with different smoothing and clipping threshold.

level of spatial correlations between the CNM structures and to mimic observations done with a limited spatial resolution, we have smoothed the data simulations by convolving them with a Gaussian function of various sizes at half maximum and analyzed the results. By doing this, it is possible to identify groups of structures that would be seen as a single object and study their properties like filling factor and velocity dispersion. We find the mass-size relation, in the bidimensional simulation, $M \propto L^{\gamma}$ with $\gamma \simeq 1.7$ and based on the assumption $\mathcal{N}(L) \propto L^{-3}$, we speculate that in 3D, we may have $M \propto L^{2.5}$. We also find that the velocity dispersion increases with the size of the structures, L, as $\sqrt{\langle \delta v^2 \rangle} \propto L^{0.4}$. These behaviour are reminiscent of the Larson laws's (Larson 1981; Heithausen et al. 1998) inferred for the molecular clouds. Moreover, since the mass spectrum that we obtain for the CNM structures in Paper II, turns out to be compatible with the mass spectrum observed for the molecular clouds (Kramer et al. 1998; Heithausen et al. 1998), this suggests that (or at least is compatible with it), the origin of the molecular clouds, is determined at a very early stage in the diffuse atomic medium. This is also consistent with the proposition made by Falgarone & Puget (1986) and recently reinvestigated by Hennebelle & Inutsuka (2006) of molecular clouds being 2-phase objects. Note that it may be at first surprising to propose a theory for the origin of molecular clouds which does not include self-gravity. However, as revealed by CO observations (e.g. Bertoldi & McKee 1992; Heyer et al. 2001), molecular clouds of mass smaller than 10^3 solar mass, are not gravitationally bound making very hard to invoke gravity as an important physical agent for the formation of these clouds. Heyer et al. (2001) also speculate that an external pressure in needed to confine them. External pressure is naturally provided by the 2-phase physics.

Finally, we have investigated the distribution of the cloud column density, $\mathcal{N}(N)$. We find that between $N \simeq 2 \times 10^{18}$ cm^{-2} and $N \simeq 2 \times 10^{19}$ cm^{-2}, $\mathcal{N}(N) \propto N^{-1.2}$ whereas from their survey, Heiles & Troland (2005) inferred $\mathcal{N}(N) \propto N^{-1}$ for $N \simeq 2 \times 10^{18}$ cm^{-2} and $N \simeq 2 \times 10^{20}$ cm^{-2}. We speculate that the discrepancy in the range of column density is due to the setup of the numerical simulation which limits the highest column densities. We also propose that the index of the power law is due to the flow being nearly scale-invariant, i.e. $\mathcal{N}(L) \propto L^{-D}$ (D being the dimension), and the CNM structures being roughly uniform in density. Whereas the first is likely to be a consequence of turbulence, the second is a consequence of the flow being thermally bistable, that is to say the density of the CNM does not change with scale or structure mass.

Acknowledgements. We acknowledge the support of the CEA computing center, CCRT, where all the simulations where carried out. We are very grateful to Snezana Stanimirović, the referee, for an insightful and constructive report which has significantly contributed to improve the paper. It is a pleasure to thank Carl Heiles and Thomas Troland for enlightening discussions on various observational aspects of the atomic interstellar medium. P.H. is grateful to Edith Falgarone and Michel Pérault, for many discussions on related topics over the years.

References

Audit, E., & Hennebelle, P. 2005, A&A, 433, 1 (Paper I)
Ballesteros-Paredes, J., Vázquez-Semadeni, E., & Goodman, A. 2002, ApJ, 571, 334
Bertoldi, F., & McKee, C. 1992, ApJ, 395, 140
Braun, R., & Kanekar, N. 2005, A&A, 436, L53
Crovisier, J. 1981, A&A, 94, 162
de Avillez, M., & Breitschwerdt, D. 2005a, A&A, 436, 585
de Avillez, M., & Breitschwerdt, D. 2005b, A&A, 634, L65
Dickey, J., & Lockman, F. 1990, ARA&A, 28, 215
Elmegreen, B. 1997, ApJ, 486, 944
Ewen, H. I., & Purcell, E. M. 1951, Nature, 168, 350
Falgarone, E., & Puget, J.-L. 1986, A&A, 162, 235
Field, G., Goldsmith, D., & Habing, H. 1969, ApJ, 155, L149
Heiles, C. 1997, ApJ, 481, 193
Heiles, C. 2001, ApJ, 551, 105
Heiles, C., & Troland, T. 2003, ApJ, 586, 1067
Heiles, C., & Troland, T. 2005, ApJ, 624, 773
Heithausen, A., Bensch, F., Stutzki, J., Falgarone, F., & Panis, J.-F. 1998, A&A, 331, L65
Heitsch, F., Burkert, A., Hartmann, L., Slyz, A., & Devriendt, J. 2005, ApJ, 633, 113
Heitsch, F., Slyz, A., Devriendt, J., Hartmann, L., & Burkert, A. 2006, ApJ, 648, 1052
Hennebelle, P., & Pérault, M. 1999, A&A, 351, 309
Hennebelle, P., & Pérault, M. 2000, A&A, 359, 1124
Hennebelle, P., & Passot, T. 2006, A&A, 448, 1083
Hennebelle, P., & Inutsuka, S.-I. 2006, ApJ, 647, 404
Hennebelle, P., & Audit, E. 2007, A&A, 465, 431
Heyer, M., Carpenter, J., & Snell, R. 2001, ApJ, 551, 852
Johnstone, S., Koribalski, B., Wilson, W., & Walker, M. 2003, MNRAS, 341, 941
Joncas, G., Boulanger, F., & Dewdney, P. E. 1992, ApJ, 397, 165
Koyama, H., & Inutsuka, S. 2000, ApJ, 532, 980
Koyama, H., & Inutsuka, S. 2002, ApJ, 564, L97
Kramer, C., Stutzki, J., Rohrig, R., & Corneliussen, U. 1998, A&A, 329, 249
Kulkarni, S. R., & Heiles, C. 1987, Interstellar processes, ed. D. Hollenbach, & H. Thronson (Reidel)
Larson, R. 1981, MNRAS, 194, 809
Lockman, F., Jahoda, K., & McCammon, D. 1986, ApJ, 302, 432
McClure-Griffiths, N., Dickey, J., Gaensler, B., et al. 2005, ApJS, 158, 178
Mac Low, M.-M., & Klessen, R. 2004, Rev. Mod. Phys., 76, 125
Miville-Deschênes, M.-A., Joncas, G., Falgarone, E., & Boulanger, F. 2003, A&A, 411, 109
Ossenkopf, V., & Mac Low, M. 2002, A&A, 390, 307
Padoan, P., & Nordlund, A. 2002, ApJ, 576, 870
Padoan, P., Goodman, A. A., & Juvela, M. 2003, ApJ, 588, 881
Rosen, A., & Bregman, J. 1995, ApJ, 470, 839
Stanimirović, S., Weisberg, A., Hedden, K., & Green, T. 2003, ApJ, 598, L23
Stanimirović, S., & Heiles, C. 2005, ApJ, 631, L371
Stil, J., Taylor, A., Dickey, J., et al. 2006, AJ, 132, 1158
Taylor, A., Gibson, S., Peracaula, M., et al. 2003, AJ, 125, 3145
Vázquez-Semadeni, E., Passot, T., & Pouquet, A. 1995, ApJ, 441, 702
Vázquez-Semadeni, E., Ryu, D., Passot, T., González, R., & Gazol, A. 2006, ApJ, 643, 245
Wolfire, M., Hollenbach, D., & McKee, C. 1995, ApJ, 443, 152
Wolfire, M., Hollenbach, D., & McKee, C. 2003, ApJ, 587, 278